

# Wide range equation of state for fluid hydrogen within density functional theory

Cong Wang<sup>1,2</sup> and Ping Zhang<sup>1,2,\*</sup>

<sup>1</sup>*Institute of Applied Physics and Computational Mathematics,  
P.O. Box 8009, Beijing 100088, People's Republic of China*

<sup>2</sup>*Center for Applied Physics and Technology,  
Peking University, Beijing 100871, People's Republic of China*

## Abstract

Wide range equation of state (EOS) for liquid hydrogen is ultimately built by combining two kinds of density functional theory (DFT) molecular dynamics simulations, namely, first-principles molecular dynamics simulations and orbital-free molecular dynamics simulations. Specially, the present introduction of short cutoff radius pseudopotentials enables the hydrogen EOS to be available in the range  $9.82 \times 10^{-4}$  to  $1.347 \times 10^3$  g/cm<sup>3</sup> and up to  $5 \times 10^7$  K. By comprehensively comparing with various attainable experimental and theoretical data, we derive the conclusion that our DFT-EOS can be readily and reliably conducted to hydrodynamic simulations of the inertial confinement fusion.

PACS numbers: 31.15.A.-, 51.30.+i, 64.30.-t

---

\*Corresponding author: zhang\_ping@iapcm.ac.cn

## I. INTRODUCTION

Wide range equation of state (EOS) for hydrogen or its isotopes is of crucial interest for inertial confinement fusion (ICF) and astrophysics [1–3]. In the traditional central-hot-spot ignition designs of ICF, a deuterium-tritium (D-T) capsule is assumed to be imploded to high density either directly by high power laser pulses [4] or indirectly by X rays generated in the hohlraum [5]. Due to the fact that the compressibility of the capsule is determined by EOS, high precision EOS of the D-T fuel is essential for hydrodynamic simulations and ignition facility designs. In astrophysics, the giant Jovian planets, such as Jupiter, Saturn, Uranus, and Neptune, are composed primarily of hydrogen and helium. The knowledge on the size and mass distribution of giant Jovian planets are sensitive to the EOS of hydrogen in a wide range [6, 7].

The EOS of hydrogen has been probed through gas gun [8], converging explosive [9], magnetically driven flyer [10], and high power laser-driven experiments [11–13], where a pressure-temperature thermodynamical domain with amplitudes of megabar (Mbar) and electron volt (eV) has been reached. Theoretical approximations, such as classical molecular dynamics based on interatomic potentials [14], linear mixing method [15], fluid variational theory (FVT) [16], path integral Monte Carlo (PIMC) [17, 18], and quantum molecular dynamics (QMD) [19, 20], have already been employed to study high-pressure behaviors of hydrogen and its isotopes. Although it has been pursued over decades, there are still some fundamental issues worth to be noticed. For instance, the first-order phase transition from molecular to atomic fluid transition is being under intense discussion, and plasma phase transition (PPT) characterized by electronic ionization still needs to be clarified [8]. High precision, wide range EOS for hydrogen are of particularly importance for hydrodynamic simulations in ICF, especially at densities from  $\sim 10^{-3}$  to  $10^3$  g/cm<sup>3</sup> and temperatures up to  $10^7$  K, or even higher. Currently, SESAME-EOS table [21, 22] for hydrogen describes chemical species, such as, H<sub>2</sub> molecules, H atoms, and free protons and electrons based on chemical models [15, 23–25], which are only expected to work well in the weak coupling limit. Recently, a new EOS table based on PIMC simulations has been built [26], however, PIMC results are not consistent with experiments at pressures below 50 GPa along the Hugoniot curve [17]. As a consequence, wide range EOS for hydrogen is highly recommended to be constructed from other promising ways for comparisons and applications.

In the present work, a combined density functional theory (DFT) method of first-principles molecular dynamics (FPMD) and orbital-free molecular dynamics (OFMD) has been used to construct wide range EOS for fluid hydrogen with a temperature range  $10^3 \sim 5 \times 10^7$  K and density range  $9.82 \times 10^{-4} \sim 1.347 \times 10^3$  g/cm<sup>3</sup>. In FPMD the electrons are treated quantum mechanically through finite-temperature DFT (FTDFT) with the only approximation of exchange-correlation functional. Due to the Fermi-Dirac distribution of the electronic states, at extremely high temperatures a huge number of occupational bands have to be introduced, and FPMD simulations are then restricted. As a consequence, OFMD simulations, where the electronic kinetic energy is expressed as a functional of the local electronic density and possibly of its gradient, have been adopted to avoid the limitation. The rest of this paper is organized as follows. Section II describes the computational methods with respect to FPMD and OFMD. In section III, we discuss the EOS in detail, and finally we get our conclusions in section IV.

## II. COMPUTATIONAL METHOD

In this section, we briefly describe the basic formalism employed to explore thermodynamic properties of fluid hydrogen. That is, two basic quantum-mechanical DFT approaches, one based on Kohn-Sham (KS) formula and the other based on orbital-free method. Then the simulation parameters are presented in detail.

### A. First-principles molecular dynamics

Our FPMD simulations for fluid hydrogen have been performed by using ABINIT code [27]. In these simulations, the electrons are fully quantum mechanically treated by employing a plane-wave FT-DFT description, where the electronic state occupations follow the Fermi-Dirac distribution. The ions move classically according to the forces from the electron density and the ion-ion repulsion. We employed the NVT (canonical) ensemble, where the number of particles  $N$  and the volume are fixed [28]. The system was assumed to be in local thermodynamic equilibrium with the electron and ion temperatures being equal ( $T_e = T_i$ ). In these calculations, the electronic temperature was been kept constant according to the Fermi-Dirac distribution, while the ionic temperature was controlled by the Noé thermostat.

At each step during MD simulations, a set of electronic state functions  $\{\Psi_{i,k}(r, t)\}$  for each  $\mathbf{k}$ -point were determined within KS construction by

$$H_{KS}\Psi_{i,k}(r, t) = \epsilon_{i,k}\Psi_{i,k}(r, t) \quad (1)$$

with

$$H_{KS} = -\frac{1}{2}\nabla^2 + V_{ext} + \int \frac{n(r')}{|r - r'|}dr' + v_{xc}(r), \quad (2)$$

in which the four terms respectively represent the kinetic contribution, the electron-ion interaction, the Hartree contribution, and the exchange-correlation functional. The electronic density was obtained by

$$n(r) = \sum_{i,k} f_{i,k} |\Psi_{i,k}(r, t)|^2. \quad (3)$$

Then by applying the velocity Verlet algorithm, based on the force from interactions between ions and electrons, a new set of positions and velocities were obtained for ions.

## B. Orbital-free molecular dynamics

OFMD simulations [29–31], where the kinetic energy of the electrons is treated semi-classically, have also been used to investigate the wide range EOS for fluid hydrogen under extreme conditions. The orbital-free electronic free energy can be expressed as

$$\begin{aligned} F_e(n) = & \frac{1}{\beta} \int dr \{n(r)\Phi(n) - \frac{2\sqrt{2}}{3\pi^2\beta^{3/2}} I_{3/2}[\Phi(n)]\} + \int dr h(n) \frac{|\nabla n|^2}{n} \\ & + F_{xc}[n] + \frac{1}{2} \int \int dr dr' \frac{n(r)n(r')}{|r - r'|} + \sum_{\ell=1}^{N_\alpha} Z_\ell \int dr \frac{n(r)}{r - R_\ell} \\ & - \mu \int dr [n(r) - \sum_{\ell=1}^{N_\alpha} Z_\ell], \end{aligned} \quad (4)$$

where  $I_\nu$  is the Fermi integral of order  $\nu$ , and the screened potential  $\Phi$  is related to the electronic density by

$$\sum_{\ell=1}^{N_\alpha} Z_\ell = \frac{\sqrt{2}}{\pi^2\beta^{3/2}} \int dr I_{1/2}(\Phi[n]). \quad (5)$$

The first integral in Eq. (4), which depends only on the local electronic density in the true spirit of the Hohenberg-Kohn theorem, is the well-known finite-temperature Thomas-Fermi expression [32]. The second term in Eq. (4) denotes the von Weizsäcker correction. In the present simulations we have omitted this gradient term and worked in a Thomas-Fermi-Dirac

form using the formula proposed by Perrot [33] to deal with the kinetic-entropic part. The orbital-free procedure treats all electrons on an equal footing, albeit approximately, with no distinction between bound and ionized electrons. Except for that, the OFMD simulation procedure is similar to that of FPMD.

### C. Simulation details

Using the above-mentioned DFT formalisms (namely, FPMD and OFMD), we aim to build a wide range DFT-EOS table of data points for liquid hydrogen with the density ranging from  $9.82 \times 10^{-4}$  to  $1.347 \times 10^3$  g/cm<sup>3</sup> and temperature from  $10^3$  to  $5 \times 10^7$  K. Generally, the Coulomb liquids can be characterized by two non-dimensional parameters. That is, the ionic coupling parameter and electronic degenerate parameter. For liquid hydrogen, the former one is commonly defined as  $\Gamma_{ii} = 1/(k_B T a)$ , which presents the ratio of the mean electrostatic potential energy and the mean kinetic energy of the ions. The degeneracy parameter  $\theta = T/T_F$  is the ratio of the temperature to the Fermi temperature  $T_F = (3/\pi^2 n_e)^{2/3}/3$ . Within the FPMD formalism, the electronic states are occupied according to the Fermi-Dirac distribution. Thus, our FPMD simulations have been restricted to temperatures lower than  $T_F$  ( $\theta < 1$ ) at  $\rho > 0.5$  g/cm<sup>3</sup>. For lower densities, our FPMD simulations have been performed up to a temperature of 15.682 eV. To overcome the computational cost limit, OFMD was used in the same simulated conditions (density and temperature) as those in FPMD, and explored to extend to higher temperatures. The results indicate that both of the pressure and internal energy difference are better than 2% between QMD and OFMD simulations as  $\theta \sim 1$  (see Fig. 1).

In general, FPMD and OFMD simulations based on DFT have introduced pseudopotentials to reduce the computational cost and ensure the accuracy at moderate densities. However, the pseudo-core approximation fails at high densities, where the interatomic distance is comparable with or smaller than the cutoff radius of the pseudopotential, due to pressure-induced delocalization of the core electrons and the overlapping of the pseudization spheres. In order to avoid the limitations introduced by pseudopotential approximation, a Columbic pseudopotential with a cutoff radius of 0.001 a.u. has been built [34, 35]. As the energy dependence is better than 1% between projector augmented wave (PAW) potentials and Columbic potential (see Fig. 2), we explore the EOS of hydrogen into high density

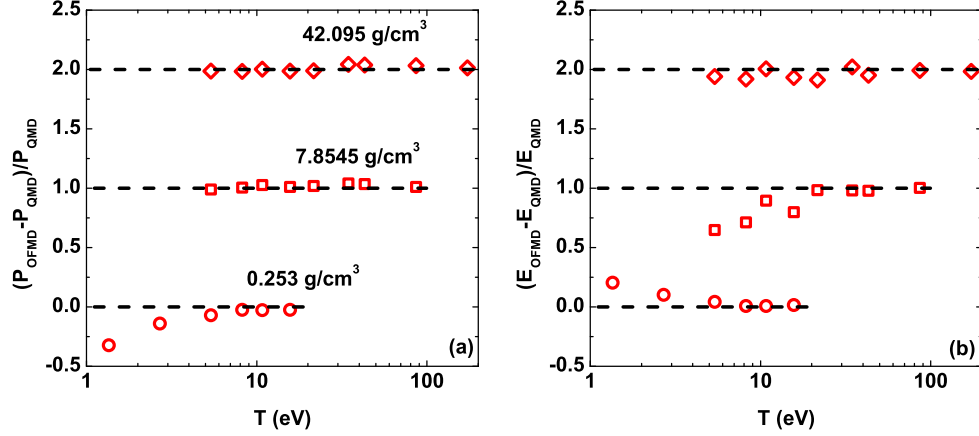


FIG. 1: (Color online) Pressure and internal energy differences between QMD and OFMD methods as functions of temperature at densities of  $0.253 \text{ g/cm}^3$  (red open circles),  $7.8545 \text{ g/cm}^3$  (red open squares), and  $42.095 \text{ g/cm}^3$  (red open diamonds). QMD results have been plotted as the black dashed line. Each curve corresponds to an isochore. Each curve has been shifted by 1.0 from the previous one for clarity.

( $\sim 10^3 \text{ g/cm}^3$ ) by using a short cutoff radius Columbic potential.

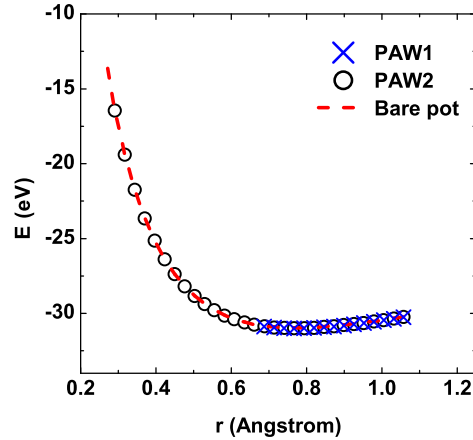


FIG. 2: (Color online) Calculated energy as a function of interatomic distance. Results are obtained from PAW potentials with a cutoff radius of 0.8 a.u. (PAW1), 0.1 a.u. (PAW2), and Columbic potential (Bare pot), as labelled in the figure.

We have considered a total number of  $8 \sim 512$  atoms (corresponding to expanded and ultra dense regimes) in a series of volume-fixed supercells, which are repeated periodically throughout the space. Only  $\Gamma$  point is used to sample the Brillouin zone in molecular

dynamic simulations, because the selection of higher number of  $\mathbf{k}$  points modifies the EOS within 3%. Each system was assumed to be in local thermodynamic equilibrium with the electron and ion temperatures being equal ( $T_i = T_e$ ). In order to balance the pseudopotential approximation in the high density regime and the computational cost, two potentials have been adopted in both FPMD and OFMD simulations. That is, the PAW (with  $R_c = 0.1$  a.u.) pseudopotential ( $\rho < 30$  g/cm<sup>3</sup>) and short cutoff radius Coulombic potential ( $\rho > 20$  g/cm<sup>3</sup>), where the plane wave cutoff energy is set to 200 Ha, respectively. The exchange-correlation functional is determined by local density approximation (LDA) with Teter-Pade parametrization [36], and the temperature dependence of exchange-correlation functional, which is convinced to be as small as negligible, is not taken into account.  $N_{step} = 6000$  has been used in the molecular dynamic simulations, and the time steps are selected with considering different density and temperature [37]. The EOS are obtained as running average of the last 1000 steps of molecular dynamic simulations. Additionally, in FPMD simulations, sufficient electronic states have been adopted to secure the occupational number below  $10^{-6}$ .

### III. RESULTS AND DISCUSSION

A wide range DFT-EOS (listed in Table I) has been constructed by data obtained from FPMD (for  $\theta < 1$ ) and OFMD ( $\theta > 1$ ) simulations. Results are compared with previous theoretical and experimental ones in this section.

TABLE I: DFT-EOS table with pressure (GPa) and internal energy (eV/atom) for hydrogen.

Temperature(eV)	Pressure(GPa)	Internal energy (eV/atom)
$\rho = 9.8200 \times 10^{-4}$ g/cm <sup>3</sup>		
1.348	0.138	6.290
2.695	0.351	13.021
5.391	0.864	26.066
8.215	1.393	35.787
10.781	1.870	46.596

to be continued on next page

TABLE I – continued from previous page

Temperature(eV)	Pressure(GPa)	Internal energy (eV/atom)
15.682	2.698	62.313
21.563	3.862	80.142
34.500	6.316	119.051
43.125	7.950	144.951
86.250	16.114	274.346
172.500	32.441	533.100
345.000	65.097	1050.593
690.000	130.407	2085.570
1293.750	244.701	3896.774
4312.500	816.153	12952.800
$\rho = 1.5590 \times 10^{-3} \text{g/cm}^3$		
1.348	0.212	6.113
2.695	0.542	12.339
5.391	1.367	25.339
8.215	2.239	35.584
10.781	3.084	45.612
15.682	4.431	61.651
21.563	6.107	79.572
34.500	10.004	118.522
43.125	12.598	144.430
86.250	25.561	273.838
172.500	51.483	532.598
345.000	103.324	1050.092
690.000	207.002	2085.071
1293.750	388.453	3896.275
4312.500	1295.667	12952.301
to be continued on next page		



TABLE I – continued from previous page

Temperature(eV)	Pressure(GPa)	Internal energy (eV/atom)
$\rho = 2.6940 \times 10^{-3} \text{g/cm}^3$		
1.348	0.359	5.927
2.695	0.908	11.683
5.391	2.298	24.074
8.215	3.827	34.673
10.781	5.188	44.264
15.682	7.739	60.708
21.563	10.493	78.773
34.500	17.231	117.794
43.125	21.715	143.715
86.250	44.118	273.146
172.500	88.912	531.914
345.000	178.498	1049.412
690.000	357.665	2084.391
1293.750	671.210	3895.596
4312.500	2238.934	12951.622
$\rho = 5.2620 \times 10^{-3} \text{g/cm}^3$		
1.348	0.676	5.732
2.695	1.710	10.860
5.391	4.316	22.440
8.215	7.278	33.087
10.781	9.943	41.650
15.682	14.981	59.245
21.563	20.322	77.561
34.500	33.495	116.710
to be continued on next page		

TABLE I – continued from previous page

Temperature(eV)	Pressure(GPa)	Internal energy (eV/atom)
43.125	42.257	142.658
86.250	86.019	272.126
172.500	173.515	530.908
345.000	348.498	1048.412
690.000	698.457	2083.394
1293.750	1310.879	3894.600
4312.500	4373.030	12950.626
$\rho = 1.2473 \times 10^{-2} \text{g/cm}^3$		
1.348	1.463	5.066
2.695	3.884	9.320
5.391	9.334	18.976
8.215	16.559	30.688
10.781	22.833	39.750
15.682	34.787	56.895
21.563	49.460	75.601
34.500	80.720	115.000
43.125	101.500	141.001
86.250	204.800	270.546
172.500	410.900	529.354
345.000	823.100	1046.868
690.000	1655.046	2081.854
1293.750	3106.100	3893.061
4312.500	10365.235	12949.087
$\rho = 2.1553 \times 10^{-2} \text{g/cm}^3$		
1.348	2.472	4.493

---

to be continued on next page

---

TABLE I – continued from previous page

Temperature(eV)	Pressure(GPa)	Internal energy (eV/atom)
2.695	6.411	8.595
5.391	16.101	18.019
8.215	27.862	29.063
10.781	38.592	37.668
15.682	59.760	55.062
21.563	84.600	73.978
34.500	138.700	113.586
43.125	174.600	139.635
86.250	353.100	269.251
172.500	709.600	528.081
345.000	1425.665	1045.603
690.000	2859.130	2080.591
1293.750	5367.606	3891.798
4312.500	17910.085	12947.823

$$\rho = 4.2095 \times 10^{-2} \text{g/cm}^3$$

1.348	4.264	4.712
2.695	12.140	8.083
5.391	30.746	16.663
8.215	52.677	27.011
10.781	73.257	35.436
15.682	112.734	52.641
21.563	162.600	71.692
34.500	268.500	111.558
43.125	339.100	137.679
86.250	682.388	267.396
172.500	1382.377	526.260

to be continued on next page

TABLE I – continued from previous page

Temperature(eV)	Pressure(GPa)	Internal energy (eV/atom)
345.000	2782.234	1043.791
690.000	5581.767	2078.781
1293.750	10481.126	3889.987
4312.500	34977.421	12946.009
$\rho = 5.0 \times 10^{-2} \text{g/cm}^3$		
1.348	5.218	4.035
2.695	14.462	7.844
5.391	33.584	17.101
8.215	62.068	26.480
10.781	86.394	34.845
15.682	133.412	50.345
21.563	192.000	71.017
34.500	318.500	110.942
43.125	401.800	137.082
86.250	809.780	266.829
172.500	1641.220	525.702
345.000	3303.920	1043.235
690.000	6629.240	2078.225
1293.750	12448.600	3889.430
4312.500	41545.000	12945.451
$\rho = 9.9781 \times 10^{-2} \text{g/cm}^3$		
0.259	2.694	0.854
0.431	3.948	1.153
0.518	4.584	1.320
0.690	5.537	1.717
to be continued on next page		

TABLE I – continued from previous page

Temperature(eV)	Pressure(GPa)	Internal energy (eV/atom)
0.863	7.924	1.836
1.348	12.306	3.131
2.695	28.755	7.031
5.391	71.782	14.766
8.215	121.424	23.631
10.781	167.717	32.418
15.682	260.606	47.720
21.563	375.300	67.930
34.500	627.300	107.984
43.125	794.300	134.196
86.250	1609.411	264.053
172.500	3268.481	522.956
345.000	6586.363	1040.493
690.000	13222.325	2075.477
1293.750	24835.110	3886.676
4312.500	82900.032	12942.686
$\rho = 1.5328 \times 10^{-1} \text{g/cm}^3$		
0.259	4.773	0.752
0.431	6.561	1.122
0.518	7.336	1.311
0.690	9.403	1.733
0.863	10.704	2.281
1.348	18.789	3.426
2.695	45.908	6.683
5.391	110.191	14.078
8.215	185.120	22.566
to be continued on next page		

TABLE I – continued from previous page

Temperature(eV)	Pressure(GPa)	Internal energy (eV/atom)
10.781	253.965	30.910
15.682	395.081	45.969
21.563	569.300	65.689
34.500	955.800	105.708
43.125	1212.000	131.937
86.250	2489.000	261.841
172.500	5013.911	520.751
345.000	10110.722	1038.280
690.000	20305.244	2073.253
1293.750	38145.083	3884.443
4312.500	127346.277	12940.439
$\rho = 1.9448 \times 10^{-1} \text{g/cm}^3$		
0.259	7.194	0.779
0.345	8.599	0.958
0.431	9.692	1.133
0.518	10.432	1.363
0.690	13.249	1.753
0.863	15.283	2.267
1.348	26.465	3.124
2.695	60.048	6.458
5.391	135.419	14.176
8.215	235.860	21.950
10.781	320.826	30.080
15.682	499.007	44.982
21.563	720.600	64.364
34.500	1209.000	104.306
to be continued on next page		

TABLE I – continued from previous page

Temperature(eV)	Pressure(GPa)	Internal energy (eV/atom)
43.125	1537.000	130.534
86.250	3158.000	260.445
172.500	6396.000	519.350
345.000	12849.073	1036.869
690.000	25809.147	2071.833
1293.750	48491.275	3883.014
4312.500	161900.916	12938.999
$\rho = 2.5301 \times 10^{-1} \text{g/cm}^3$		
0.259	11.871	0.798
0.345	13.700	0.975
0.431	15.444	1.162
0.518	16.105	1.451
0.690	18.874	1.889
0.863	22.934	2.267
1.348	36.898	3.296
2.695	82.165	6.293
5.391	186.413	13.224
8.215	298.231	21.654
10.781	414.411	29.201
15.682	643.852	43.913
21.563	924.300	62.908
34.500	1562.000	102.714
43.125	1984.000	128.927
86.250	4094.000	258.819
172.500	8293.000	517.709
345.000	16672.990	1035.209
to be continued on next page		

TABLE I – continued from previous page

Temperature(eV)	Pressure(GPa)	Internal energy (eV/atom)
690.000	33498.380	2070.157
1293.750	62944.837	3881.326
4312.500	210176.125	12937.294
$\rho = 3.3676 \times 10^{-1} \text{g/cm}^3$		
0.259	22.170	0.881
0.345	24.459	1.064
0.431	24.239	1.349
0.518	26.790	1.617
0.690	31.156	1.949
0.863	37.359	2.291
1.348	57.070	3.257
2.695	117.535	6.153
5.391	255.253	12.911
8.215	414.266	20.725
10.781	566.886	28.198
15.682	852.768	42.767
21.563	1220.000	61.324
34.500	2066.000	100.926
43.125	2627.000	127.094
86.250	5430.000	256.931
172.500	10984.218	515.784
345.000	22178.636	1033.253
690.000	44572.273	2068.174
1293.750	83762.886	3879.325
4312.500	279722.953	12935.268

---

to be continued on next page

---



TABLE I – continued from previous page

Temperature(eV)	Pressure(GPa)	Internal energy (eV/atom)
$\rho = 4.1867 \times 10^{-1} \text{g/cm}^3$		
0.086	28.457	0.666
0.259	36.339	0.954
0.431	36.579	1.480
0.690	47.351	2.009
0.863	55.779	2.342
1.348	81.633	3.291
2.695	156.889	6.117
5.391	326.268	12.694
8.215	522.548	20.335
10.781	685.171	27.621
15.682	1058.104	41.926
21.563	1515.000	60.154
34.500	2562.000	99.553
43.125	3267.000	125.671
86.250	6744.000	255.430
172.500	13690.000	514.238
345.000	27562.538	1031.671
690.000	55403.077	2066.565
1293.750	104128.019	3877.696
4312.500	347756.729	12933.615
$\rho = 5.0 \times 10^{-1} \text{g/cm}^3$		
0.086	43.727	0.739
0.259	49.036	1.148
0.431	53.691	1.583
0.690	68.576	2.092
to be continued on next page		

TABLE I – continued from previous page

Temperature(eV)	Pressure(GPa)	Internal energy (eV/atom)
0.863	79.054	2.419
1.348	110.256	3.352
2.695	203.690	6.226
5.391	403.036	12.590
8.215	634.218	20.070
10.781	854.595	27.285
15.682	1293.154	41.537
21.563	1799.000	59.237
34.500	3020.820	98.444
43.125	3844.600	124.507
86.250	7984.900	254.174
172.500	16287.600	512.930
345.000	32907.200	1030.326
690.000	66155.400	2065.190
1293.750	124347.000	3876.302
4312.500	415320.000	12932.195

$$\rho = 7.9825 \times 10^{-1} \text{g/cm}^3$$

1.348	259.313	3.792
2.695	404.291	6.492
5.391	718.712	12.638
8.215	1077.005	19.843
10.781	1423.714	26.707
15.682	2108.910	40.544
21.563	2905.275	57.192
34.500	4831.500	95.738
43.125	6136.150	121.574

to be continued on next page

TABLE I – continued from previous page

Temperature(eV)	Pressure(GPa)	Internal energy (eV/atom)
86.250	12721.700	250.794
172.500	25961.000	509.293
345.000	52483.001	1026.515
690.000	105556.001	2061.257
1293.750	198451.502	3872.289
4312.500	662975.008	12928.083
$\rho = 9.8181 \times 10^{-1} \text{g/cm}^3$		
1.348	384.866	4.176
2.695	560.854	6.845
5.391	944.470	12.880
8.215	1382.305	19.957
10.781	1796.059	26.734
15.682	2632.108	40.258
21.563	3678.614	57.308
34.500	5871.477	93.996
43.125	7456.522	120.184
86.250	15556.243	252.157
172.500	31880.886	512.898
345.000	64517.773	1030.922
690.000	129799.546	2065.866
1293.750	244056.648	3876.955
4312.500	815392.161	12932.766
$\rho=1.2263 \text{ g/cm}^3$		
1.348	591.578	4.774
2.695	811.125	7.441
to be continued on next page		

TABLE I – continued from previous page

Temperature(eV)	Pressure(GPa)	Internal energy (eV/atom)
5.391	1282.332	13.347
8.215	1816.492	20.228
10.781	2324.122	26.844
15.682	3353.252	40.091
21.563	4638.863	56.811
34.500	7391.677	92.514
43.125	9309.797	118.716
86.250	19393.895	250.119
172.500	39770.389	510.828
345.000	80525.778	1028.729
690.000	162054.556	2063.622
1293.750	304757.918	3874.666
4312.500	1018329.725	12930.412
$\rho=1.5591 \text{ g/cm}^3$		
2.695	1217.205	8.329
5.391	1802.722	14.093
8.215	2471.084	20.813
10.781	3107.909	27.280
15.682	4394.780	40.431
21.563	6008.367	56.715
34.500	9711.442	94.365
43.125	11868.865	117.384
86.250	24627.130	248.026
172.500	50504.260	508.563
345.000	102305.520	1026.416
690.000	205947.039	2061.235
to be continued on next page		

TABLE I – continued from previous page

Temperature(eV)	Pressure(GPa)	Internal energy (eV/atom)
1293.750	387371.949	3872.216
4312.500	1294596.497	12927.871
$\rho=2.0241 \text{ g/cm}^3$		
2.695	1914.054	9.701
5.391	2653.269	15.315
8.215	3499.908	21.844
10.781	4303.718	28.115
15.682	5940.816	40.924
21.563	8003.076	56.885
34.500	12739.349	93.854
43.125	15981.851	119.108
86.250	31973.372	245.712
172.500	65497.743	505.963
345.000	132718.486	1023.755
690.000	267252.973	2058.470
1293.750	502770.574	3869.360
4312.500	1680568.581	12924.885
$\rho=3.6956 \text{ g/cm}^3$		
2.695	5561.156	15.030
5.391	6851.582	20.465
8.215	8282.303	26.503
10.781	9683.735	32.433
15.682	12471.118	44.273
21.563	16109.020	59.548
34.500	24440.344	94.995
to be continued on next page		

TABLE I – continued from previous page

Temperature(eV)	Pressure(GPa)	Internal energy (eV/atom)
43.125	30151.959	119.149
86.250	58805.086	239.239
172.500	119458.718	500.123
345.000	241975.435	1017.331
690.000	487450.871	2051.576
1293.750	917350.383	3862.109
4312.500	3067567.944	12917.150
$\rho=5.0 \text{ g/cm}^3$		
2.695	9549.150	19.264
5.391	11289.594	24.705
8.215	13149.412	30.532
10.781	14947.198	36.149
15.682	18635.588	47.707
21.563	23350.696	62.524
34.500	33750.403	94.172
43.125	41345.121	119.872
86.250	80760.602	244.172
172.500	162974.601	496.972
345.000	329461.530	1026.672
690.000	662036.697	2067.672
1293.750	1243990.000	3869.013
4312.500	4152780.000	12918.432
$\rho=7.8545 \text{ g/cm}^3$		
5.391	23919.083	32.364
8.215	26366.144	35.213
to be continued on next page		

TABLE I – continued from previous page

Temperature(eV)	Pressure(GPa)	Internal energy (eV/atom)
10.781	28417.191	40.201
15.682	34567.155	50.461
21.563	40887.110	63.836
34.500	57821.094	96.066
43.125	69405.461	118.905
86.250	129424.016	240.005
172.500	257431.789	492.021
345.000	517526.963	968.205
690.000	1040160.000	2052.492
1293.750	1953890.000	3857.032
4312.500	6522980.000	12881.855

$$\rho = 1.2473 \times 10^1 \text{ g/cm}^3$$

5.391	52334.071	45.782
8.215	56804.007	50.849
10.781	60424.429	54.502
15.682	68219.429	62.075
21.563	77112.745	74.889
34.500	103991.965	105.034
43.125	121078.467	127.234
86.250	213335.193	245.844
172.500	412180.825	487.534
345.000	823130.585	1015.634
690.000	1652820.000	2028.342
1293.750	3103200.000	3841.490
4312.500	10356600.000	12898.888

---

to be continued on next page

---

TABLE I – continued from previous page

Temperature(eV)	Pressure(GPa)	Internal energy (eV/atom)
$\rho = 2.1553 \times 10^1 \text{ g/cm}^3$		
5.391	132965.313	69.516
8.215	140631.941	75.069
10.781	147606.997	79.707
15.682	161508.892	91.188
21.563	176692.441	98.682
34.500	214260.781	124.801
43.125	244807.793	144.762
86.250	397368.524	255.511
172.500	733042.082	498.257
345.000	1436410.000	1015.776
690.000	2860880.000	2037.937
1293.750	5365630.000	3849.903
4312.500	17899300.000	12890.991
$\rho = 4.2095 \times 10^1 \text{ g/cm}^3$		
5.391	420619.812	120.275
8.215	436741.892	121.507
10.781	445038.475	125.749
15.682	477946.889	134.127
21.563	500374.227	144.655
34.500	574053.275	169.598
43.125	621244.176	187.496
86.250	900873.051	288.390
172.500	1516040.000	519.066
345.000	2861940.000	996.990
690.000	5626920.000	2054.507
to be continued on next page		



TABLE I – continued from previous page

Temperature(eV)	Pressure(GPa)	Internal energy (eV/atom)
1293.750	10503500.000	3853.605
4312.500	34970300.000	12898.971
$\rho = 8.4190 \times 10^1 \text{ g/cm}^3$		
5.391	1380830.000	197.188
8.215	1405720.000	199.217
10.781	1437320.000	206.732
15.682	1491360.000	217.589
21.563	1546100.000	223.268
34.500	1657160.000	252.920
43.125	1765120.000	269.112
86.250	2250500.000	359.484
172.500	3390870.000	572.109
345.000	5962050.000	1047.419
690.000	11406900.000	2049.414
1293.750	21127400.000	3824.306
4312.500	69971100.000	12895.733
$\rho = 1.6838 \times 10^2 \text{ g/cm}^3$		
5.391	4470890.000	348.905
8.215	4531710.000	353.258
10.781	4567730.000	357.249
15.682	4706480.000	365.018
21.563	4754720.000	374.545
34.500	5038440.000	396.244
43.125	5235950.000	411.271
86.250	6139410.000	492.918
to be continued on next page		

TABLE I – continued from previous page

Temperature(eV)	Pressure(GPa)	Internal energy (eV/atom)
172.500	8286640.000	684.142
345.000	13024000.000	1128.948
690.000	23505400.000	2101.594
1293.750	42790700.000	3685.375
4312.500	140264000.000	12902.503
$\rho = 3.3676 \times 10^2 \text{ g/cm}^3$		
5.391	14545500.000	588.613
8.215	14665000.000	591.546
10.781	14723000.000	599.508
15.682	14995000.000	602.836
21.563	15179700.000	616.630
34.500	15789200.000	636.221
43.125	16093600.000	650.506
86.250	17859500.000	726.080
172.500	21530900.000	897.457
345.000	30504600.000	1301.652
690.000	50560500.000	2224.865
1293.750	87731800.000	3952.434
4312.500	281715000.000	12945.568
$\rho = 6.7352 \times 10^2 \text{ g/cm}^3$		
5.391	47188700.000	985.291
8.215	47374300.000	989.586
10.781	47542300.000	993.478
15.682	47866200.000	1000.964
21.563	48258700.000	1010.034
to be continued on next page		

TABLE I – continued from previous page

Temperature(eV)	Pressure(GPa)	Internal energy (eV/atom)
34.500	49138100.000	1030.355
43.125	49735000.000	1044.162
86.250	52836300.000	1115.850
172.500	59610600.000	1272.441
345.000	75258300.000	1634.074
690.000	112078000.000	2485.051
1293.750	183785000.000	4142.350
4312.500	566346000.000	12930.233
$\rho = 1.3470 \times 10^3 \text{ g/cm}^3$		
5.391	152939000.000	1629.645
8.215	153307000.000	1633.926
10.781	153649000.000	1637.809
15.682	152494000.000	1645.251
21.563	155067000.000	1654.214
34.500	156786000.000	1674.139
43.125	157956000.000	1687.602
86.250	163941000.000	1756.777
172.500	176641000.000	1903.589
345.000	204903000.000	2230.145
690.000	271115000.000	2995.092
1293.750	405010000.000	4541.812
4312.500	1154030000.000	12958.110

### A. Hugoniot curve

High precision EOS data are essential for understanding target implosion process in ICF. We first examine the present DFT-EOS theoretically through the Rankine-Hugoniot (RH)

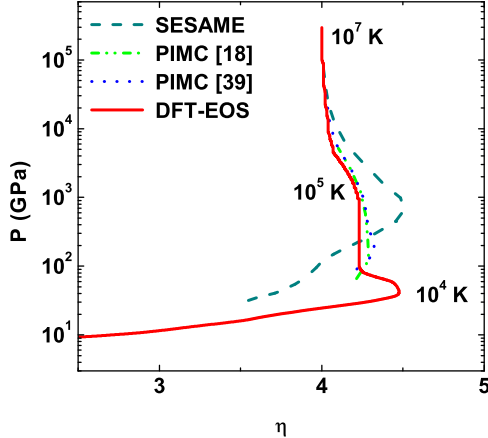


FIG. 3: (Color online) Present DFT-EOS for wide-range Hugoniot curve (red line) of liquid hydrogen. Previous wide-range Hugoniot curves from PIMC simulations (by S. X. Hu *et al.* [38] and Militzer *et al.* [18]) and SESAME [21] are also shown for comparison.

equations, which follow from conservation of mass, momentum, and energy across the front of the shock wave. The locus of points in  $(E, P, V)$ -space described by RH equations satisfy

$$E_1 - E_0 = \frac{1}{2}(P_1 + P_0)(V_1 - V_0), \quad (6)$$

$$(P_1 - P_0) = \rho_0 u_s u_p, \quad (7)$$

$$V_1 = V_0(1 - u_p/u_s), \quad (8)$$

where subscripts 0 and 1 represent the initial and shocked state, and  $E$ ,  $P$ , and  $V$  denote internal energy, pressure, and volume, respectively.  $u_p$  is the particle velocity of the material behind the shock front and  $u_s$  is the shock velocity. Along the Hugoniot curve of the liquid hydrogen, the starting point with a density of  $0.0855 \text{ g/cm}^3$  and a temperature of 23 K has been selected, where the relative internal energy has been set to zero and the pressure is considered as small as negligible. Smooth functions have been adopted to fit DFT-EOS in the relative density and temperature regime. Our DFT-based Hugoniot curve with pressure up to  $10^5$  GPa and temperature up to  $5 \times 10^7$  K is presented in Fig. 3. Our simulation results indicate that the maximum shock compression ratio is 4.5 with a pressure around 40 GPa, at which the system is governed by gradual dissociation of molecules. With the increase of pressure, the compression ratio decreases and then reaches a value of 4.23 below 950 GPa. This hardening behavior of the Hugoniot can be attributed to the formation

of mono-atomic fluid. However, as the pressure exceeds  $10^3$  GPa (temperature above 19 eV), the compression ratio merges into 4.0, which indicate a full ionization of the liquid hydrogen. On the other side, SESAME Hugoniot [21] plotted in Fig. 3 shows a maximum compression ratio around 4.5, but the corresponding pressure is much too high with respect to our DFT-Hugoniot. For comparison, previous results from PIMC simulations [18, 38] are also plotted in Fig. 3, which shows consistency with our DFT results at pressures beyond 50 GPa. However, PIMC simulations have failed to reproduce the experimental results below 50 GPa.

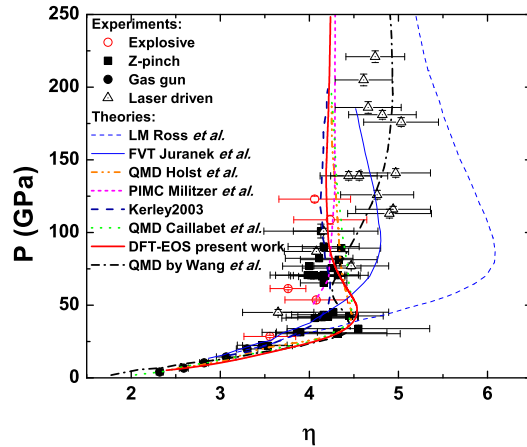


FIG. 4: (Color online) Hugoniot curve based on present DFT-EOS for liquid hydrogen with (red solid line) or without (red dashed line) considering ionic quantum zero-point energy. Previous experimental results and theoretical predictions are shown for comparison. Experimental data: gas gun by Nellis *et al.* [8] (solid circles), Z-pinch by Knudson *et al.* [10] (solid squares), explosives of Boriskov *et al.* [9] (open circles), laser-driven by Hicks *et al.* [13] (up open triangles), and Boehly *et al.* [12] (down open triangles). Theoretical data: QMD simulation results by Holst *et al.* (orange line) [39], Caillabet *et al.* (green line) [40], and Wang *et al.* (black dash-dotted line) [41], PIMC results by Militzer *et al.* (magenta line) [18], Kerley (royal line) [22], LM model by Ross (blue dashed line) [15], and FVT (blue solid line) [25].

Over the past ten years, the Hugoniot of hydrogen or deuterium has been experimentally explored up to  $\sim 200$  GPa. The latest set of data points were obtained by two-stage light gas gun [8], explosive-driven compression [9], Z-pinch-driven compression [10], where the compression ratio  $\eta$  shows a maximum close to 4.3, or by laser-driven compression with the Nova laser and the Omega laser (the EOS would possibly be corrected by introducing the

quartz standard), which suggest a stiff behavior ( $\eta_{max} \approx 4.2$ ) below 100 GPa and become softer ( $\eta_{max} \approx 4.5 \sim 5.5$ ) at higher pressures [12, 13]. To clearly show the comparison between the present DFT-EOS and those previous results, Fig. (4) plots the Hugoniot curve below 250 GPa. The present Hugoniot curve from DFT-EOS with accounting for the ionic quantum zero-point energy (ZPE) shows better accordance with experimental data. At pressures below 100 GPa, both of the curves, as discussed above, exhibit a maximum compression ratio of 4.5, which is accordant with previous QMD results and experimental data obtained by gas gun, converging explosives and magnetically driven flyer. However, as pressures go beyond 100 GPa,  $\eta \sim 4.3$  indicates the agreement with high power laser experiments with the quartz standard. Predictions from various chemical models are also shown for comparison, for instance, Kerley 2003 [22], linear mixing model [15], and the fluid variational theory (FVT) [25]. Those chemical methods generally predict larger maximum compression ratio into higher pressures, except for the Kerley 2003 EOS, which is in better agreement with experiments.

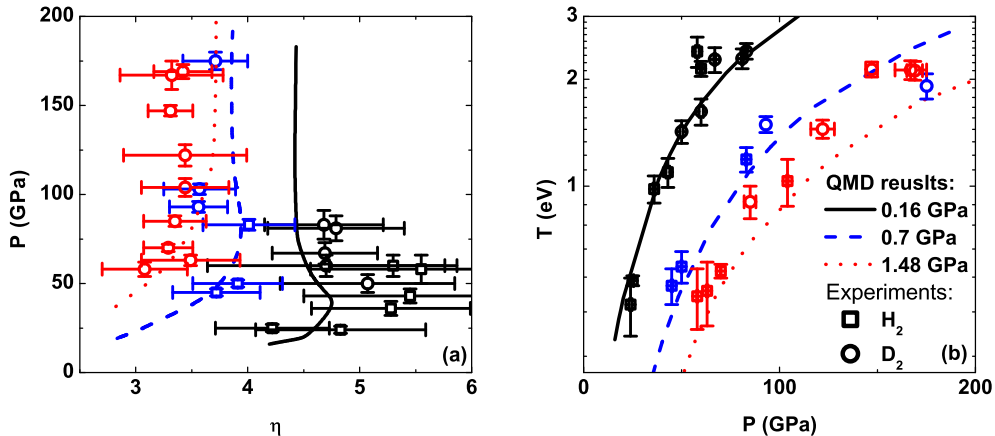


FIG. 5: (Color online) Pressure versus compression ratio (a) and temperature versus pressure (b). For comparison with the most recent experimental data [42], three initial pre-compressions of  $H_2$  ( $D_2$ ) samples at 297 K have been studied: 0.16 GPa, 0.7 GPa, and 1.48 GPa.

Recently, laser-driven shock compressions on  $H_2$  or  $D_2$  precompressed in diamond anvil cells from 0.16 to 1.6 GPa have been proved to provide visible ways to generate shock Hugoniot data over a significantly broader thermodynamical regime than previous experiments [42]. These experimental data are highly valuable for examining various theoretical models. In the present work, we have shown the Hugoniot data for initial pre-compressions of 0.16

GPa, 0.7 GPa, and 1.48 GPa in Fig. 5. As a consequence, the data covers a density range  $\sim 2$  times greater than previous investigations limited to the principal Hugoniot alone. As shown in Fig. 5, good agreement has been gained between the present DFT-EOS pre-compressed Hugoniot data and laser-driven experimental results. The maximum compression ratio along a given Hugoniot has been observed to strongly depend on the initial density. That is, with increasing initial density, the compression ratio decreases.

## B. Molecular dissociations

For molecular fluid in the warm dense regime, which consists of atoms, molecules, nuclei, and electrons, the free energy can be expressed as

$$F(\rho, T) = F_{id}^{(i)} + F_{id}^{(e)} + F_{ex}^{(i-e)} + F_{dis}^{(mol)}, \quad (9)$$

where  $F_{id}^{(i)}$  and  $F_{id}^{(e)}$  are the ideal free energies for ions and electrons, respectively,  $F_{ex}^{(i-e)}$  is the excess free energy, while  $F_{dis}^{(mol)}$  denotes the contribution from molecular dissociation with the following form [40]:

$$F_{dis}^{(mol)} = Nk_B T \left\{ \ln \alpha + \frac{1 - \alpha}{2} \right\}. \quad (10)$$

Here the dissociation ratio  $\alpha$  is used as an adjustable function of density and temperature, with an assumed Fermi-function form

$$\alpha(\rho, T) = \frac{1}{\exp[B(\rho)/T - C(\rho)T] + 1}, \quad (11)$$

where  $B(\rho) = \exp(B_1 + B_2\rho)$  and  $C(\rho) = \exp(C_1 + C_2\rho)$ . Using the present DFT-EOS data, we have determined the value  $B_1 = 9.5517$ ,  $B_2 = -2.8277$ ,  $C_1 = -8.2946$ , and  $C_2 = 0.4708$ .

At temperatures below 10000 K, molecular dissociation governs the first-order phase transition, which is important in determining the nonmetal-to-metal transition. In this work, we have introduced a Fermi formula to fit our DFT-EOS in warm dense region by using Eq. (11), and the dissociation fraction has been plotted in Fig. 6. Vorberger *et al.* [43] have introduced a criteria to estimate the fraction of molecular hydrogen by counting the number of atoms located within a radius, which last for a time greater than ten vibrational periods. Holst *et al.* [39] have used a coordination number,

$$K(r) = \frac{N - 1}{V} \int_0^r 4\pi r'^2 g(r') dr', \quad (12)$$

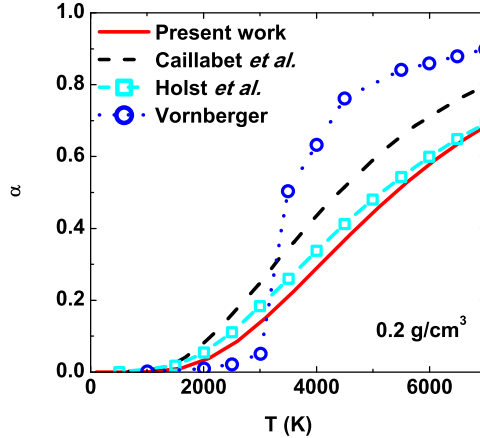


FIG. 6: (Color online) Calculated molecular dissociation fraction as a function of temperature at  $0.2 \text{ g/cm}^3$ . For comparison, previous theoretical results [39, 40, 43] have also been plotted.

to determine  $\alpha$ , where  $g(r)$  is the pair correlation function to present the possibility of finding a particle from a reference atom. Results from those different assumptions are compared with the present work in Fig. 6. They yield similar tendency with temperature at the sampled density. The dissociation fraction from Vorberger *et al.* strongly depends on the definition of the molecule in this region, and shows abrupt increase as temperature increases. However, QMD method gives a smoother behavior of  $\alpha$  as indicated in Fig. 6.

### C. Comparison of DFT-EOS with previous theoretical results

In this section, the present DFT-EOS data have been systemically compared with previous theoretical predictions. At densities from  $\sim 10^{-3} \text{ g/cm}^3$  to  $\sim 10^{-1} \text{ g/cm}^3$ , we have shown the pressure and internal energy difference between our DFT-EOS and those obtained by PIMC simulations (see Fig. 7). The results indicate a maximum of 7% difference for the pressure and 15% for the energy over the temperatures we explore. At temperatures above  $\sim 30 \text{ eV}$ , the distinction can be viewed as small as negligible between the two methods. In the warm dense regime, which is highlighted at densities between  $0.2$  and  $3.0 \text{ g/cm}^3$ , very good agreement has been found between our DFT-EOS data and those fitted QMD results at the temperature domain  $2000 \sim 10000 \text{ K}$  (left panel in Fig. 8). At temperature beyond  $10000 \text{ K}$ , results from PIMC simulations by Militzer *et al.* [18], Chabrier Model [44], and QMD simulations [39, 40] have been plotted in the right panel in Fig. 8. The PIMC method



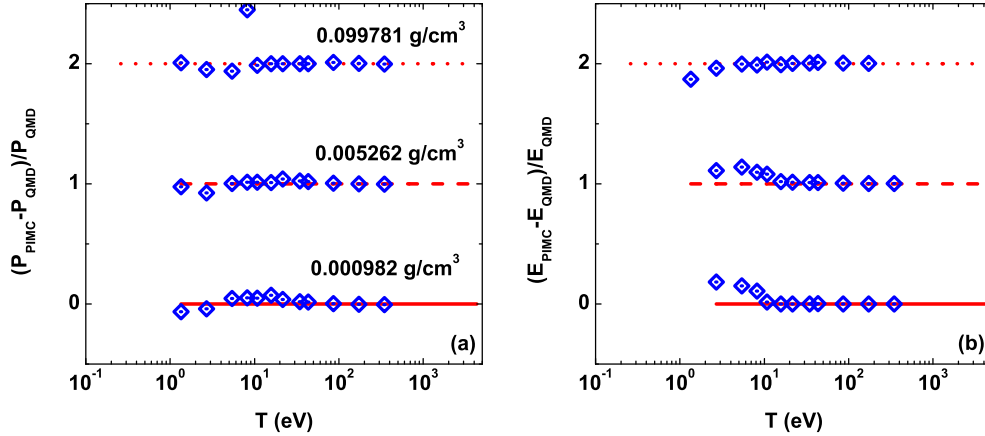


FIG. 7: (Color online) Pressure (a) and internal energy (b) differences between QMD and PIMC [26] methods as functions of temperature. QMD results are plotted as the red solid, red dashed, and red dotted lines at densities of 0.000982, 0.005262, and 0.099781 g/cm<sup>3</sup>, respectively. The blue open diamonds denote PIMC data. Each curve corresponds to an isochores. Each curve has been shifted by 1.0 from the previous one for clarity.

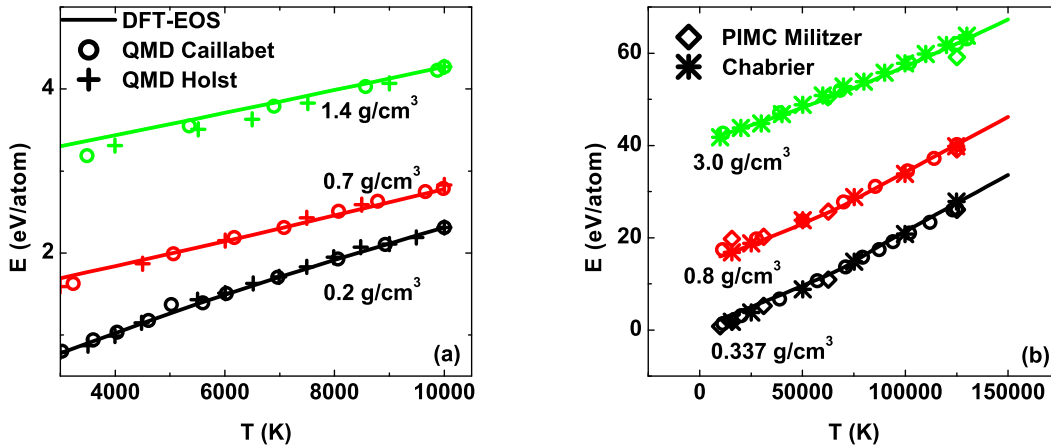


FIG. 8: (Color online) Internal energy of liquid hydrogen as a function of temperature. Previous QMD [39, 40], PIMC [18], and Chabrier model [44] results are also shown for comparison.

is suitable for investigating many-body quantum systems at high temperatures. In this method, electrons and ions are treated on equal footing as paths. The model of Chabrier and Potekhin considers a fully ionized plasma, which is reliable at high temperature and low density region. As shown in Fig. 8, the present results are in accordance with those numerical simulations and theoretical models.

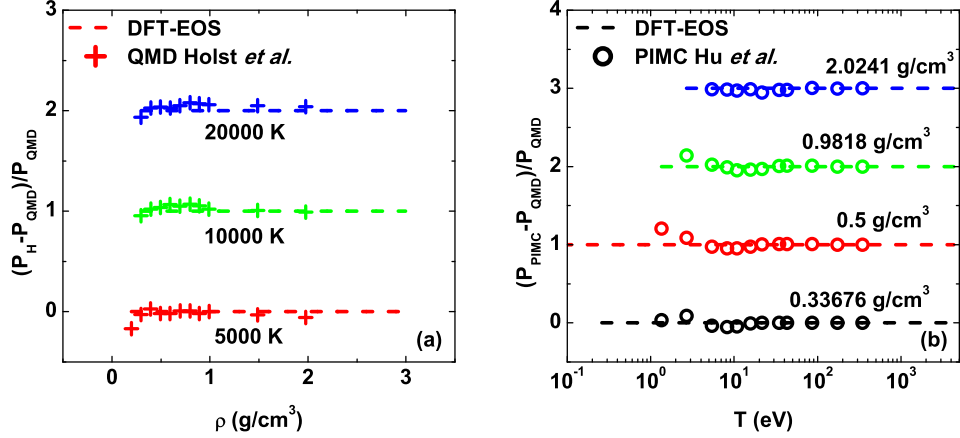


FIG. 9: (Color online) (a) Pressure difference as a function of density,  $P_H$  denotes data from Holst *et al.* [39]; (b) Pressure difference as a function of temperature,  $P_{\text{PIMC}}$  are obtained from Hu *et al.* [26]. Each curve has been shifted by 1.0 from the previous one for clarity.

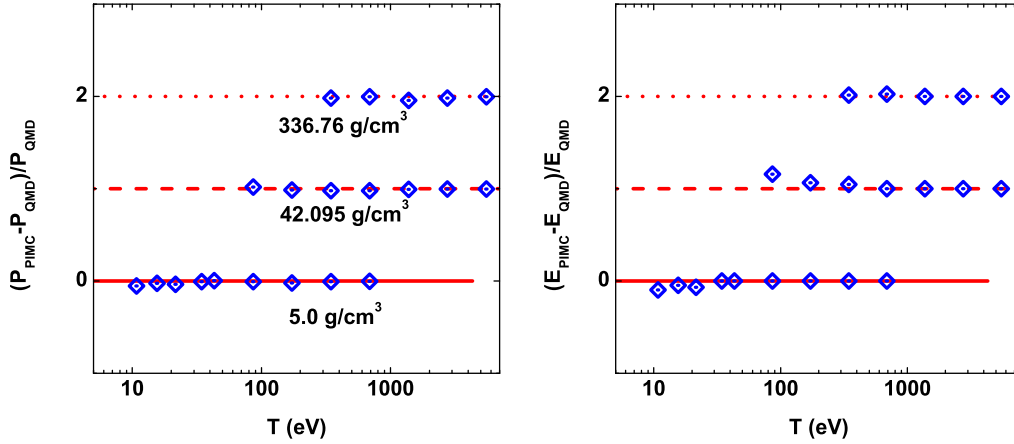


FIG. 10: (Color online) DFT-EOS is compared with PIMC data [26] in the dense plasma region. The present DFT-EOS results are shown as red lines, and blue open diamonds denote PIMC data. Each curve has been shifted by 1.0 from the previous one for clarity.

The isotherms of the pressure have been observed to show a systematic behavior in terms of the density and temperature (see Fig. 9). In this region, we do not find any signs for  $(\frac{\partial P}{\partial V})_T > 0$ , which would indicate another first-order phase transition (the so-called PPT). PPT is usually considered in chemical models such as fluid variational theory [25] or liquid state perturbation theory [45]. In these chemical models, minimization of the free energy for a mixture consists of atoms, molecules, and plasma in equilibrium. Relations

between different particles are described by effective potentials. As we explore to a higher temperature region (right panels in Fig. 9 and Fig. 10), PIMC data by Hu *et al.* [26] are shown for comparison. It is clearly indicated that the pressure given by DFT-EOS is in good agreement with PIMC calculations up to  $\sim 10^7$  K for the densities concerned, and this agreement extends toward lower temperatures when the density decreases.

#### IV. CONCLUSION

In summary, we have constructed a wide-range DFT-EOS by means of FPMD and OFMD simulations. After building short cutoff radius Columbic potential, we have the ability to explore the EOS into ultra-dense region. The present DFT-EOS is valid at densities from  $9.82 \times 10^{-4}$  to  $1.347 \times 10^3$  g/cm<sup>3</sup> with the temperature up to  $5 \times 10^7$  K. Available experimental data and theoretical models have been introduced to compare with current DFT-EOS. We have found good agreement between our results and those data probed by gas gun, chemical explosive, and magnetic driven plate flyer experiments, which indicate a maximum compression ratio of 4.5 around 40 GPa. At higher pressures, our data show stiff behavior and validates the high power laser experiments with quartz standard. The principal Hugoniot curve is also accordant with previous QMD simulation results. Agreement has also been found between our DFT-EOS Hugoniot data and those obtained by pre-compressed laser-driven shock wave experiments, which provide visible ways to generate EOS in a broader density and temperature regime. As density and temperature enter into a denser and hotter regime, where experimental detections are prohibited, the present results are compared with those predicted by chemical model and PIMC simulations. The present DFT-EOS covers typical states as can be reached in ICF and will be applied in hydrodynamic simulations in the future work.

#### V. ACKNOWLEDGEMENT

This work was supported by NSFC under Grants No. 11275032, No. 11005012 and No. 51071032, by the National Basic Security Research Program of China, and by the National High-Tech ICF Committee of China.

- 
- [1] S. Atzeni and J. Meyer-ter-Vehn, *The Physics of Inertial Fusion: Beam Plasma Interaction, Hydrodynamics, Hot Dense Matter*, International Series of Monographs on Physics (Clarendon Press, Oxford, 2004).
- [2] T. Guillot, *Science* **286**, 72 (1999).
- [3] T. Guillot, *Planet. Space Sci.* **47**, 1183 (1999).
- [4] R. L. McCrory, *et al.* *Phys. Plasmas* **15**, 055503 (2008).
- [5] J. D. Lindl, *Phys. Plasmas* **2**, 3933 (1995).
- [6] W. B. Hubbard, *Science* **214**, 145 (1980).
- [7] D. J. Stevenson, *Annu. Rev. Earth Planet. Sci.* **10**, 257 (1982).
- [8] W. J. Nellis, *Rep. Prog. Phys.* **69**, 1479 (2006).
- [9] G. V. Boriskov, A. I. Bykov, R. Ilkaev, V. D. Selemir, G. V. Simakov, R. F. Trunin, V. D. Urlin, A. N. Shuikin, and W. J. Nellis, *Phys. Rev. B* **71**, 092104 (2005).
- [10] M. D. Knudson, D. L. Hanson, J. E. Bailey, C. A. Hall, J. R. Asay, and C. Deeney, *Phys. Rev. B* **69**, 144209 (2004).
- [11] G. W. Collins, L. B. Da Silva, P. Celliers, D. M. Gold, M. E. Ford, R. J. Wallace, A. Ng, S. V. Weber, K. S. Budil, and R. Cauble, *Science* **281**, 1178 (1998).
- [12] T. R. Boehly, D. G. Hicks, P. M. Celliers, T. J. B. Collins, R. Earley, J. H. Eggert, D. Jacobs-Perkins, S. J. Moon, E. Vianello, D. D. Meyerhofer, and G. W. Collins, *Phys. Plasmas* **11**, L49 (2004).
- [13] D. G. Hicks, T. R. Boehly, P. M. Celliers, J. H. Eggert, S. J. Moon, D. D. Meyerhofer, and G. W. Collins, *Phys. Rev. B* **79**, 014112 (2009).
- [14] A. B. Belonoshko, A. Rosengren, N. V. Skorodumova, S. Bastea, and B. Johansson, *J. Chem. Phys.* **122**, 124503 (2005).
- [15] M. Ross, *Phys. Rev. B* **58**, 669 (1998).
- [16] H. Juranek and R. Redmer, *J. Chem. Phys.* **112**, 3780 (2000).
- [17] W. R. Magro, D. M. Ceperley, C. Pierleoni, and B. Bernu, *Phys. Rev. Lett.* **76**, 1240 (1996).
- [18] B. Militzer and D. M. Ceperley, *Phys. Rev. Lett.* **85**, 1890 (2000).
- [19] V. Bezkrovniy, V. S. Filinov, D. Kremp, M. Bonitz, M. Schlanges, W. D. Kraeft, P. R. Levashov, and V. E. Fortov, *Phys. Rev. E* **70**, 057401 (2004).

- [20] T. Lenosky, S. Bickham, J. Kress, and L. Collins, Phys. Rev. B **61**, 0163 (2000).
- [21] G. I. Kerley, Phys. Earth Planet. Inter. **6**, 78 (1972).
- [22] G. I. Kerley, Sandia National Laboratory, Albuquerque, NM, Report SAND2003-3613 (2003).
- [23] D. Saumon and G. Chabrier, Phys. Rev. A **46**, 2084 (1992).
- [24] F. J. Rogers, Contrib. Plasma Phys. **41**, 179 (2001).
- [25] H. Juranek, R. Redmer, and Y. Rosenfeld, J. Chem. Phys. **117**, 1768 (2002).
- [26] S. X. Hu, B. Militzer, V. N. Goncharov, and S. Skupsky, Phys. Rev. B **84**, 224109 (2011).
- [27] ABINIT (available at [www.abinit.org](http://www.abinit.org)) is a common project of the Université Catholique de Louvain (Louvain-la Neuve, Belgium), Corning Incorporated, and other contributors.
- [28] J. M. Haile, Molecular Dynamics Simulation (Wiley-Interscience, New York, 1997).
- [29] F. Lambert, J. Cléroutin, and S. Mazevet, Europhys. Lett. **75**, 681 (2006).
- [30] S. Mazevet, F. Lambert, F. Bottin, G. Zérah, and J. Cléroutin, Phys. Rev. E **75**, 056404 (2007).
- [31] F. Lambert, J. Cléroutin, J.-F. Danel, L. Kazandjian, and G. Zérah, Phys. Rev. E **77**, 026402 (2008).
- [32] M. Brack and R. K. Bhaduri, Semiclassical Physics (Westview, Oxford, 2003).
- [33] F. Perrot, Phys. Rev. A **20**, 586 (1979).
- [34] C. Wang, X.-T. He, and P. Zhang, Phys. Rev. Lett. **106**, 145002 (2011).
- [35] C. Wang, X.-T. He, and P. Zhang, Phys. Plasmas **19**, 042702 (2012).
- [36] S. Goedecker, M. Teter, J. Huetter, Phys. Rev. B **54**, 1703 (1996).
- [37] The time steps have been taken as  $\Delta t = a/20\sqrt{k_B T/m_H}$ , where  $a = (3/4\pi n_i)^{1/3}$  is the ionic sphere radius ( $n_i$  is the ionic number density),  $k_B T$  presents the kinetic energy, and  $m_H$  is the ionic hydrogen.
- [38] S. X. Hu, B. Militzer, V. N. Goncharov, and S. Skupsky, Phys. Rev. Lett. **104**, 235003 (2010).
- [39] B. Holst, R. Redmer, and M. P. Desjarlais, Phys. Rev. B **77**, 184201 (2008).
- [40] L. Caillabet, S. Mazevet, and P. Loubeyre, Phys. Rev. B **83**, 094101 (2011).
- [41] C. Wang, X.-T. He, and P. Zhang, J. Appl. Phys. **108**, 044909 (2010).
- [42] P. Loubeyre, S. Btygoo, J. Eggert, P. M. Celliers, D. K. Spaulding, J. R. Rygg, T. R. Boehly, G. W. Collins, and R. Jeanloz, Phys. Rev. B **86**, 144115 (2012).
- [43] J. Vorberger, I. Tamblyn, B. Militzer, and S. A. Bonev, Phys. Rev. B **75**, 024206 (2007).
- [44] G. Chabrier and A. Y. Potekhin, Phys. Rev. E **58**, 4941 (1998).
- [45] D. Saumon, G. Chabrier, and H. M. van Horn, Astrophys. J. Suppl. Ser. **99**, 713 (1995).